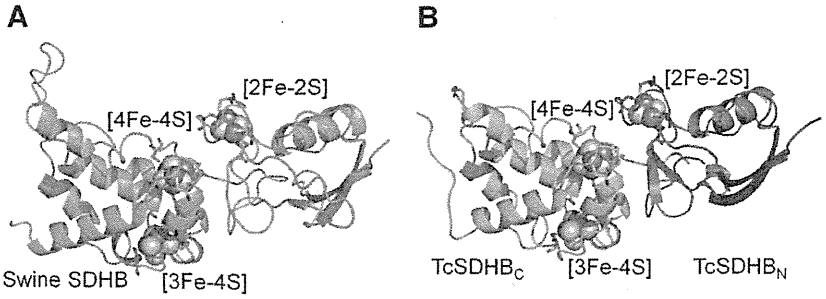

Fig. 8. PHYRE^2 model of split *T. cruzi* SDHB subunits. Superposition of porcine SDHB crystal structure (green, residues Pro B9 to Glu B237) (A), with the PHYRE^2 model of *T. cruzi* SDHB$_N$ (pink, residues Thr B$_N$66 to Asp B$_N$161) and SDHB$_C$ (blue, residues Val B$_C$34 to Pro B$_C$163) subunits (B). All cysteine residues coordinating with the Fe–S clusters are conserved and represented as stick, while iron (orange) and sulfur (yellow) clusters as spheres. The C-terminal residues from B$_N$162 to B$_N$270 of TcSDHB$_N$ were removed from the PHYRE^2 model for ease of comparison between porcine and *T. cruzi* SDHB subunits.

of the 5′-upstream regions of complex II genes identified putative hypoxia-responsive element (HREs), suggesting that HIF-1 directly regulates the expression of stage-specific complex II isoforms [43].

Diversity of complex II is found not only in parasites but also in human host. Two isoforms of human Fp, type I and type II, were reported [44,45]. These isoforms differed from each other only in two amino acid residues: Tyr 586 and Val 614 of type I Fp are replaced by Phe 586 and Ile 614 in type II Fp, respectively. Type I Fp are well conserved among the Fp of mammals, and type II Fp is found only in human complex II. Although the type I Fp gene is located on chromosome 5p15 and has an exon–intron structure [44,46], the type II Fp gene is not found in the NCBI database. Baysal et al. suggested that type II Fp is a variant of the Fp subunit and can be explained by balancing selection over the long term [47]. Interestingly, expression of type II Fp mRNA is increased in normal cells cultured under ischemic conditions [48]. It is of interest to speculate that complex II^{II} has higher QFR activity and plays an important role in fumarate respiration in human mitochondria as the terminal oxidase of the system similar to that in *A. suum* adult complex II. Anti-cancer activity of pyrvinium pamoate an anthelmintic, which is a known fumarate reductase inhibitor, against human cancer cells should be studied further [49]. The diversity of mitochondrial complex II molecules lends itself to studies in many areas, including bioenergetics, molecular evolution and drug discovery.

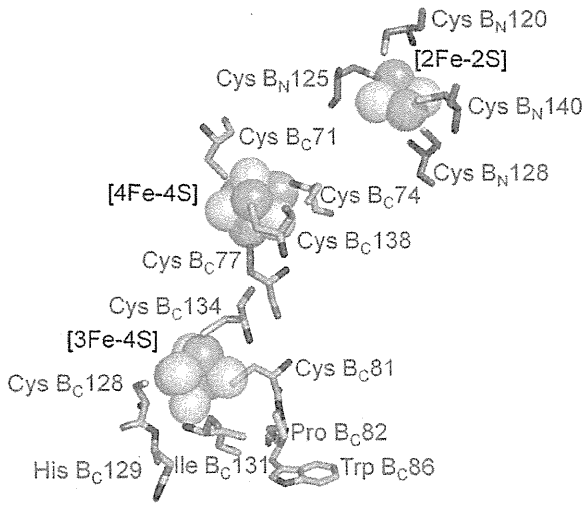

Fig. 9. All cysteines necessary for binding Fe–S clusters are conserved in Trypanosomal split Ip subunits. Cysteine residues from SDHB$_N$ are colored and labeled in pink and residues from SDHB$_C$ are in blue. The equivalent residues from Trypanosomal SDHB$_C$, which were found to interact with flutolanil from porcine SDHB are labeled in red. The three iron (orange) and sulfur (yellow) clusters are represented as spheres.

Acknowledgments

This work was supported in part by Programme for the Promotion of Basic and Applied Researches for Innovations in Bio-oriented Industry (BRAIN), a Creative Scientific Research Grant 18GS0314, a Grant-in-Aid for Scientific Research on Priority Areas 18073004 from the Japanese Society for the Promotion of Science, and the Targeted Proteins Research Program of the Japanese Ministry of Education, Science, Culture, Sports and Technology (MEXT).

References

[1] K. Kita, H. Hirawake, S. Takamiya, Cytochromes in the respiratory chain of helminth mitochondria, Int. J. Parasitol. 27 (1997) 617–630.
[2] R. Komuniecki, P.R. Komuniecki, Aerobic–anaerobic transitions in energy metabolism during the development of the parasitic nematode *Ascaris suum*, in: J.C. Boothroyd, R. Komuniecki (Eds.), Molecular Approaches to Parasitology, Wiley-Liss, Inc., New York, 1995, pp. 109–121.
[3] A.G.M. Tielens, C. Rotte, J.J. van Hellemond, W. Martin, Mitochondria as we don't know them, Trends Biochem. Sci. 27 (2002) 56–72.
[4] K. Kita, S. Takamiya, Electron-transfer complexes in *Ascaris* mitochondria, Adv. Parasitol. 51 (2002) 95–131.
[5] K. Kita, Electron-transfer complexes in *Ascaris suum*, Parasitol. Today 8 (1992) 155–159.
[6] H. Amino, A. Osanai, H. Miyadera, N. Shinjyo, E. Tomitsuka, H. Taka, R. Mineki, K. Murayama, S. Takamiya, T. Aoki, H. Miyoshi, K. Sakamoto, S. Kojima, K. Kita, Isolation and characterization of the stage-specific cytochrome *b* small subunit (CybS) of *Ascaris suum* complex II from the aerobic respiratory chain of larval mitochondria, Mol. Biochem. Parasitol. 128 (2003) 175–186.
[7] H. Amino, H. Wang, H. Hirawake, F. Saruta, D. Mizuchi, R. Mineki, N. Shindo, K. Murayama, S. Takamiya, T. Aoki, S. Kojima, K. Kita, Stage specific isoforms of *Ascaris suum* complex II: the fumarate reductase of the parasitic adult and the succinate dehydrogenase of free-living larvae share a common iron–sulfur subunit, Mol. Biochem. Parasitol. 106 (2000) 63–76.
[8] K. Kita, H. Hirawake, H. Miyadera, H. Amino, S. Takeo, Role of complex II in anaerobic respiration of the parasite mitochondria from *Ascaris suum* and *Plasmodium falciparum*, Biochim. Biophys. Acta 1553 (2002) 123–139.
[9] S. Omura, H. Miyadera, H. Ui, K. Shiomi, Y. Yamaguchi, R. Masuma, T. Nagamitsu, D. Takano, T. Sunazuka, A. Harder, H. Kölbl, M. Namikoshi, H. Miyoshi, K. Sakamoto, K. Kita, An anthelmintic compound, nafuredin, shows selective inhibition of complex I in helminth mitochondria, Proc. Natl. Acad. Sci. U. S. A. 98 (2001) 60–62.
[10] F. Saruta, T. Kuramochi, K. Nakamura, S. Takamiya, Y. Yu, T. Aoki, K. Sekimizu, S. Kojima, K. Kita, Stage-specific isoforms of complex II (succinate–ubiquinone oxidoreductase) in mitochondria from the parasitic nematode, *Ascaris suum*, J. Biol. Chem. 270 (1995) 928–932.
[11] S. Takamiya, K. Kita, H. Wang, P.P. Weinstein, A. Hiraishi, H. Oya, T. Aoki, Developmental changes in the respiratory chain of *Ascaris* mitochondria, Biochim. Biophys. Acta 1141 (1993) 65–74.
[12] S.T. Cole, C. Condon, B.D. Lemire, J.H. Weiner, Molecular biology, biochemistry and bioenergetics of fumarate reductase, a complex membrane-bound iron–sulfur flavoenzyme of *Escherichia coli*, Biochim. Biophys. Acta 811 (1985) 381–403.
[13] H. Miyadera, A. Hiraishi, H. Miyoshi, K. Sakamoto, R. Mineki, K. Murayama, K.V. Nagashima, K. Matsuura, S. Kojima, K. Kita, Complex II from phototrophic purple bacterium *Rhodoferax fermentans* displays rhodoquinol–fumarate reductase activity, Eur. J. Biochem. 270 (2003) 1863–1874.

[14] M. Heinz, Encyclopedic Reference of Parasitology, second ed. Springer, Berlin 2001.
[15] F. Iwata, N. Shinjyo, H. Amino, K. Sakamoto, M.K. Islam, N. Tsuji, K. Kita, Change of subunit composition of mitochondrial complex II (succinate-ubiquinone reductase/quinol-fumarate reductase) in *Ascaris suum* during migration in the experimental host, Parasitol. Int. 57 (2008) 54–61.
[16] C. Hägerhäll, Succinate: quinone oxidoreductases: variations on a conserved theme, Biochim. Biophys. Acta 1320 (1997) 107–141.
[17] R.S. Lemos, A.S. Fernandes, M.M. Pereira, C.M. Gomes, M. Teixeira, Quinol:fumarate oxidoreductases and succinate:quinone oxidoreductase: phylogenetic relationships, metal centres and membrane attachment, Biochim. Biophys. Acta 1553 (2002) 158–170.
[18] T.M. Iverson, C. Luna-Chavez, G. Cecchini, D.C. Rees, Structure of the *Escherichia coli* fumarate reductase respiratory complex, Science 284 (1999) 1961–1966.
[19] C.R.D. Lancaster, A. Kröger, M. Auer, H. Michel, Structure of fumarate reductase from *Wolinella succinogenes* at 2.2 Å resolution, Nature 402 (1999) 377–385.
[20] H. Shimizu, A. Osanai, K. Sakamoto, D.K. Inaoka, T. Shiba, S. Harada, K. Kita, Crystal structure of mitochondrial quinol–fumarate reductase from the parasitic nematode *Ascaris suum*, J. Biochem. 151 (2012) 589–592.
[21] V. Yankovskaya, R. Horsefield, S. Törnroth, C. Luna-Chavez, H. Miyoshi, C. Léger, B. Byrne, G. Cecchini, S. Iwata, Architecture of succinate dehydrogenase and reactive oxygen species generation, Science 299 (2003) 700–704.
[22] F. Sun, X. Huo, Y. Zhai, A. Wang, J. Xu, D. Su, M. Bartlam, Z. Rao, Crystal structure of mitochondrial respiratory membrane protein complex II, Cell 121 (2005) 1043–1057.
[23] L. Huang, G. Sun, D. Cobessi, A.C. Wang, J.T. Shen, E.Y. Tung, V.E. Anderson, E.A. Berry, 3-Nitropropionic acid is a suicide inhibitor of mitochondrial respiration that, upon oxidation by complex II, forms a covalent adduct with a catalytic base arginine in the active site of the enzyme, J. Biol. Chem. 281 (2006) 5965–5972.
[24] J. Morales, T. Mogi, S. Mineki, E. Takashima, R. Mineki, H. Hirawake, K. Sakamoto, S. Ōmura, K. Kita, Novel mitochondrial complex II isolated from *Trypanosoma cruzi* is composed of twelve peptides including a heterodimeric Ip subunit, J. Biol. Chem. 284 (2009) 7255–7263.
[25] T. Mogi, K. Kita, Identification of mitochondrial complex II subunits SDH3 and SDH4 and ATP synthase subunits a and b in *Plasmodium* spp, Mitochondrion 9 (2009) 443–453.
[26] A. Osanai, S. Harada, K. Sakamoto, H. Shimizu, D.K. Inaoka, K. Kita, Crystallization of mitochondrial rhodoquinol-fumarate reductase from the parasitic nematode *Ascaris suum* with the specific inhibitor flutolanil, Acta Crystallogr., Sect. F: Struct. Biol. Cryst. Commun. 65 (2009) 941–944.
[27] K. Motoba, M. Uchida, E. Tada, Mode of antifungal action and selectivity of flutolanil, Agric. Biol. Chem. 52 (1988) 1445–1449.
[28] C.C. Page, C.C. Moser, X. Chen, P.L. Dutton, Natural engineering principles of electron tunnelling in biological oxidation-reduction, Nature 402 (1999) 47–52.
[29] T.M. Tomasiak, T.L. Archuleta, J. Andrell, C. Luna-Chavez, T.A. Davis, M. Sarwar, A.J. Ham, W.H. McDonald, V. Yankovskaya, H.A. Stern, J.N. Johnston, E. Maklashina, G. Cecchini, T.M. Iverson, Geometric restraint drives on- and off-pathway catalysis by the *Escherichia coli* menaquinol:fumarate reductase, J. Biol. Chem. 286 (2011) 3047–3056.
[30] P. Taylor, S.L. Pealing, G.A. Reid, S.K. Chapman, M.D. Walkinshaw, Structural and mechanistic mapping of a unique fumarate reductase, Nat. Struct. Biol. 6 (1999) 1108–1112.
[31] D.K. Inaoka, K. Sakamoto, H. Shimizu, T. Shiba, G. Kurisu, T. Nara, T. Aoki, K. Kita, S. Harada, Structures of *Trypanosoma cruzi* dihydroorotate dehydrogenase complexed with substrates and products: atomic resolution insights into mechanisms of dihydroorotate oxidation and fumarate reduction, Biochemistry 47 (2008) 10881–10891.
[32] World Health Organization Report of the first meeting of WHO Strategic and Technical Advisory Group on Neglected Tropical Diseases, WHO, Geneva, Switzerland, 2007.
[33] N.M. El-Sayed, P.J. Myler, D.C. Bartholomeu, D. Nilsson, G. Aggarwal, A.N. Tran, E. Ghedin, E.A. Worthey, A.L. Delcher, G. Blandin, S.J. Westenberger, E. Caler, G.C. Cerqueira, C. Branche, B. Haas, A. Anupama, E. Amer, L. Aslund, P. Attipoe, E. Bontempi, F. Bringaud, P. Burton, E. Cadag, D.A. Campbell, M. Carrington, J. Crabtree, H. Darban, J.F. da Silveira, P. de Jong, K. Edwards, P.T. Englund, G. Fazelina, T. Feldblyum, M. Ferella, A.C. Frasch, K. Gull, D. Horn, L. Hou, Y. Huang, E. Kindlund, M. Klingbeil, S. Kluge, H. Koo, D. Lacerda, M.J. Levin, H. Lorenzi, T. Louie, C.R. Machado, R. McCulloch, A. McKenna, Y. Mizuno, J.C. Mottram, S. Nelson, S. Ochaya, K. Osoegawa, G. Pai, M. Parsons, M. Pentony, U. Pettersson, M. Pop, J.L. Ramirez, J. Rinta, L. Robertson, S.L. Salzberg, D.O. Sanchez, A. Seyler, R. Sharma, J. Shetty, A.J. Simpson, E. Sisk, M.T. Tammi, R. Tarleton, S. Teixeira, S. Van Aken, C. Vogt, P.N. Ward, B. Wickstead, J. Wortman, O. White, C.M. Fraser, K.D. Stuart, B. Andersson, The genome sequence of *Trypanosoma cruzi*, etiologic agent of Chagas disease, Science 309 (2005) 409–415.
[34] M. Berriman, E. Ghedin, C. Hertz-Fowler, G. Blandin, H. Renauld, D.C. Bartholomeu, N.J. Lennard, E. Caler, N.E. Hamlin, B. Haas, U. Böhme, L. Hannick, M.A. Aslett, J. Shallom, L. Marcello, L. Hou, B. Wickstead, U.C. Alsmark, C. Arrowsmith, R.J. Atkin, A.J. Barron, F. Bringaud, K. Brooks, M. Carrington, I. Cherevach, T.J. Chillingworth, C. Churcher, L.N. Clark, C.H. Corton, A. Cronin, R.M. Davies, J. Doggett, A. Djikeng, T. Feldblyum, M.C. Field, A. Fraser, I. Goodhead, Z. Hance, D. Harper, B.R. Harris, H. Hauser, J. Hostetler, A. Ivens, K. Jagels, D. Johnson, J. Johnson, K. Jones, A.X. Kerhornou, H. Koo, N. Larke, S. Landfear, C. Larkin, V. Leech, A. Line, A. Lord, A. Macleod, P.J. Mooney, S. Moule, D.M. Martin, G.W. Morgan, K. Mungall, H. Norbertczak, D. Ormond, G. Pai, C.S. Peacock, J. Peterson, M.A. Quail, E. Rabbinowitsch, M.A. Rajandream, C. Reitter, S.L. Salzberg, M. Sanders, S. Schobel, S. Sharp, M. Simmonds, A.J. Simpson, L. Tallon, C.M. Turner, A. Tait, A.R. Tivey, S. Van Aken, D. Walker, D. Wanless, S. Wang, B. White, O. White, S. Whitehead, J. Woodward, J. Wortman, M.D. Adams, T.M. Embley, K. Gull, E. Ullu, J.D. Barry, A.H. Fairlamb, F. Opperdoes, B.G. Barrell, J.E. Donelson, N. Hall, C.M. Fraser, S.E. Melville, N.M. El-Sayed, The genome of the African trypanosome *Trypanosoma brucei*, Science 309 (2005) 416–422.
[35] A.C. Ivens, C.S. Peacock, E.A. Worthey, L. Murphy, G. Aggarwal, M. Berriman, E. Sisk, M.A. Rajandream, E. Adlem, R. Aert, A. Anupama, Z. Apostolou, P. Attipoe, N. Bason, C. Bauser, A. Beck, S.M. Beverley, G. Bianchettin, K. Borzym, G. Bothe, C.V. Bruschi, M. Collins, E. Cadag, L. Ciarloni, C. Clayton, R.M. Coulson, A. Cronin, A.K. Cruz, R.M. Davies, J. De Gaudenzi, D.E. Dobson, A. Duesterhoeft, G. Fazelina, N. Fosker, A.C. Frasch, A. Fraser, M. Fuchs, C. Gabel, A. Goble, A. Goffeau, D. Harris, C. Hertz-Fowler, H. Hilbert, D. Horn, Y. Huang, S. Klages, A. Knights, M. Kube, N. Larke, L. Litvin, A. Lord, T. Louie, M. Marra, D. Masuy, K. Matthews, S. Michaeli, J.C. Mottram, S. Müller-Auer, H. Munden, S. Nelson, H. Norbertczak, K. Oliver, S. O'neil, M. Pentony, T.M. Pohl, C. Price, B. Purnelle, M.A. Quail, E. Rabbinowitsch, R. Reinhardt, M. Rieger, J. Rinta, J. Robben, L. Robertson, J.C. Ruiz, S. Rutter, D. Saunders, M. Schäfer, J. Schein, D.C. Schwartz, K. Seeger, A. Seyler, S. Sharp, H. Shin, D. Sivam, R. Squares, S. Squares, V. Tosato, C. Vogt, G. Volckaert, R. Wambutt, T. Warren, H. Wedler, J. Woodward, S. Zhou, W. Zimmermann, D.F. Smith, J.M. Blackwell, K.D. Stuart, B. Barrell, P.J. Myler, The genome of the kinetoplastid parasite, *Leishmania major*, Science 309 (2005) 436–442.
[36] L.A. Kelley, M.J. Sternberg, Protein structure prediction on the Web: a case study using the Phyre server, Nat. Protoc. 4 (2009) 363–371.
[37] V.G. Grivennikova, E.V. Gavrikova, A.A. Timoshin, A.D. Vinogradov, Fumarate reductase activity of bovine heart succinate-ubiquinone reductase. New assay system and overall properties of the reaction, Biochim. Biophys. Acta 1140 (1993) 282–292.
[38] E. Maklashina, G. Cecchini, Comparison of catalytic activity and inhibitors of quinone reactions of succinate dehydrogenase (Succinate-ubiquinone oxidoreductase) and fumarate reductase (Menaquinol-fumarate oxidoreductase) from *Escherichia coli*, Arch. Biochem. Biophys. 369 (1999) 223–232.
[39] H. Miyadera, K. Shiomi, H. Ui, Y. Yamaguchi, R. Masuma, H. Tomoda, H. Miyoshi, A. Osanai, K. Kita, S. Omura, Atpenins, potent and specific inhibitors of mitochondrial complex II (succinate-ubiquinone oxidoreductase), Proc. Natl. Acad. Sci. U. S. A. 100 (2003) 473–477.
[40] Y. Kido, K. Sakamoto, K. Nakamura, M. Harada, T. Suzuki, Y. Yabu, H. Saimoto, F. Yamakura, D. Ohmori, A. Moore, S. Harada, K. Kita, Purification and kinetic characterization of recombinant alternative oxidase from *Trypanosoma brucei brucei*, Biochim. Biophys. Acta 1797 (2010) 443–450.
[41] B.E. Baysal, R.E. Ferrell, J.E. Willett-Brozick, E.C. Lawrence, D. Myssiorek, A. Bosch, A. van der Mey, P.E. Taschner, W.S. Rubinstein, E.N. Myers, C.W. Richard, C.J. Cornelisse, P. Devilee, B. Devlin, Mutations in SDHD, a mitochondrial complex II gene, in hereditary paraganglioma, Science 287 (2000) 848–851.
[42] G.L. Semenza, Oxygen sensing, homeostasis, and disease, N. Engl. J. Med. 365 (2011) 537–547.
[43] M. Goto, H. Amino, M. Nakajima, N. Tsuji, K. Sakamoto, K. Kita, Cloning and characterization of hypoxia-inducible factor-1 subunits from *Ascaris suum* - a parasitic nematode highly adapted to changes of oxygen conditions during its life cycle, Gene (in press), http://dx.doi.org/10.1016/j.gene.2012.12.025.
[44] E. Tomitsuka, H. Hirawake, Y. Goto, M. Taniwaki, S. Harada, K. Kita, Direct evidence for two distinct forms of the flavoprotein subunit of human mitochondrial complex II (succinate-ubiquinone reductase), J. Biochem. 134 (2003) 191–195.
[45] E. Tomitsuka, Y. Goto, M. Taniwaki, K. Kita, Direct evidence for expression of type II flavoprotein subunit in human complex II (succinate-ubiquinone reductase), Biochem. Biophys. Res. Commun. 311 (2003) 774–779.
[46] T. Bourgeron, P. Rustin, D. Chretien, M. Birch-Machin, M. Bourgeois, E. Viegas-Péquignot, A. Munnich, A. Rötig, Mutation of a nuclear succinate dehydrogenase gene results in mitochondrial respiratory chain deficiency, Nat. Genet. 11 (1995) 144–149.
[47] B.E. Baysal, E.C. Lawrence, R.E. Ferrell, Sequence variation in human succinate dehydrogenase genes: evidence for long-term balancing selection on SDHA, BMC Biol. 5 (2007) 12.
[48] C. Sakai, E. Tomitsuka, H. Esumi, S. Harada, K. Kita, Mitochondrial fumarate reductase as a target of chemotherapy: from parasites to cancer cells, Biochim. Biophys. Acta 1820 (2012) 643–651.
[49] E. Tomitsuka, K. Kita, H. Esumi, An anticancer agent, pyrvinium pamoate inhibits the NADH-fumarate reductase system—a unique mitochondrial energy metabolism in tumour microenvironments, J. Biochem. 152 (2012) 171–183.

Unraveling the Heater: New Insights into the Structure of the Alternative Oxidase

Anthony L. Moore,[1] Tomoo Shiba,[2] Luke Young,[1] Shigeharu Harada,[3] Kiyoshi Kita,[2] and Kikukatsu Ito[4]

[1]Biochemistry and Molecular Biology, School of Life Sciences, University of Sussex, Brighton BN1 9QG, United Kingdom; email: a.l.moore@sussex.ac.uk

[2]Department of Biomedical Chemistry, Graduate School of Medicine, University of Tokyo, Tokyo 113-0033, Japan

[3]Department of Applied Biology, Graduate School of Science and Technology, Kyoto Institute of Technology, Kyoto 606-8585, Japan

[4]Cryobiofrontier Research Center, Faculty of Agriculture, Iwate University, Morioka 020-8550, Japan

Annu. Rev. Plant Biol. 2013. 64:637–63

The *Annual Review of Plant Biology* is online at plant.annualreviews.org

This article's doi:
10.1146/annurev-arplant-042811-105432

Keywords

electron transport, cytochrome pathway, diiron carboxylate proteins, respiration, ubiquinol oxidase, NADH dehydrogenases

Abstract

The alternative oxidase is a membrane-bound ubiquinol oxidase found in the majority of plants as well as many fungi and protists, including pathogenic organisms such as *Trypanosoma brucei*. It catalyzes a cyanide- and antimycin-A-resistant oxidation of ubiquinol and the reduction of oxygen to water, short-circuiting the mitochondrial electron-transport chain prior to proton translocation by complexes III and IV, thereby dramatically reducing ATP formation. In plants, it plays a key role in cellular metabolism, thermogenesis, and energy homeostasis and is generally considered to be a major stress-induced protein. We describe recent advances in our understanding of this protein's structure following the recent successful crystallization of the alternative oxidase from *T. brucei*. We focus on the nature of the active site and ubiquinol-binding channels and propose a mechanism for the reduction of oxygen to water based on these structural insights. We also consider the regulation of activity at the posttranslational and retrograde levels and highlight challenges for future research.

Contents

INTRODUCTION

The alternative oxidase (AOX) is a terminal ubiquinol oxidase that in eukaryotes is located on the substrate side of the cytochrome bc_1 complex in the mitochondrial respiratory chain. It is virtually ubiquitous within the plant kingdom and is also found in many fungi and protists, including pathogenic organisms such as *Trypanosoma brucei* and *Cryptosporidium parvum*. Homologs have also been identified in α-proteobacteria and are emerging in a broad range of animal species, and its distant relative, the plastid terminal oxidase, has been identified in cyanobacteria (75). The functions of AOXs are highly diverse and typically include thermogenesis, stress tolerance (particularly to stresses induced by the generation of reactive oxygen species), and the maintenance of mitochondrial and cellular homeostasis, to name but a few (40).

AOX has been widely researched, yet until recently we knew very little about its three-dimensional structure. Knowledge of the structure-function relationships of AOX is fundamental to a fuller understanding of how the protein operates in planta and, in particular, its role in regulating plant growth and development. The ability of the plant cell to maintain energy homeostasis, particularly under biotic and abiotic stresses, is central to plant survival under such conditions. To understand the roles that AOX plays in defending against such metabolic fluctuations, we need to determine how its structure enables it to perform such functions.

A long-term pursuit in AOX research has been the identification of suitable expression and purification conditions to facilitate the crystallization of the protein. In this review, we restrict our discussion to the recent structural insights into AOXs following the crystallization of the trypanosomal alternative oxidase (TAO) along with how changes in structure might influence function. For fuller descriptions of the function and regulation of AOX both in vitro and in vivo, readers are referred to other reviews and publications (4, 40, 61, 77, 78, 98, 117, 124, 125).

AOX: alternative oxidase

TAO: trypanosomal alternative oxidase

HISTORICAL PERSPECTIVES

The observation that plants can raise their temperature above the ambient temperature (i.e., are thermogenic) was first published in 1778 by Lamarck (73), who noted that the spadices of certain plants (Araceae) were "hot to the point of boiling" (pp. 537–38). Approximately 100 years later, in an 1877 letter to his friend the Marchese Corsi-Salviati, the illustrious explorer and botanist Dr. Eduardo Beccari reported his discovery of a gigantic aroid (*Amorphophallus titanum*) in Sumatra (12, 55). These findings were confirmed in 1885 by Henry Forbes (see 55), who stumbled across this magnificent plant during his wanderings in

the eastern archipelago. Beccari subsequently sent tubers and seeds of this plant to the Marchese in Florence. Unfortunately, the tubers did not arrive owing to import restrictions in Marseilles, but the seeds did, and under careful supervision they germinated in the Marchese's garden. On Beccari's request, young plants were transported to Kew Gardens, and the first *Amorphophallus* flowering outside of its native Sumatra occurred in June 1889.

Aroids were not the only plants to be observed to have thermogenic properties. For instance, in 1851 Garreau (47) noted a close relationship between respiration and heat development, and in 1855 Caspary (26) demonstrated that the flower temperature of *Victoria regia* rose 15°C above ambient during flowering and noted that "the chemical process that is happening at that moment is a very vivid process which has been called 'burning' and that the source of heat is due to oxygen intake" (p. 753)—a remarkable conclusion given the simplicity of the measurements. In 1898 Miyake (83) observed that the flowering of *Nelumbo nucifera* was also associated with a temperature rise of 10°C above ambient. Even today, botanical gardens around the world continue to cultivate thermogenic plants because of the great publicity and crowds they draw.

Even given the tremendous insights of Garreau (47), Caspary (26), and Miyake (83), however, the cause of the heat generation by thermogenic plants remained a mystery until 150 years after Lamarck's discovery, when Van Herk (126–128) discovered that respiration in Araceae spadices was remarkably insensitive to inhibition by cyanide and suggested that this could be due to the activity of a respiratory pathway containing a noncytochrome autooxidizable flavoprotein. The suggestion that cyanide-insensitive respiration is due to a second respiratory pathway that branches from the main respiratory chain on the substrate side of cytochrome *c* arose from Okunuki's (93) investigations during his study of pollen respiration. James & Beevers (62) extended Van Herk's observations to *Arum maculatum*, and James & Elliott (63) demonstrated that cyanide-insensitive respiration is indeed mitochondrial in origin.

The presence of an auto-oxidizable flavoprotein remained one of the best explanations for the mechanism of heat generation by cyanide-resistant respiration until Bendall & Bonner (15) reviewed the area and the various proposed hypotheses and concluded, in light of new results, that although a flavoprotein was in many ways the most plausible solution, it could not account for the observation that simple flavoprotein oxidases reduce oxygen to hydrogen peroxide rather than water. They further concluded that because the cyanide-resistant respiration could be inhibited by metal chelators, either a nonheme iron or another type of metalloprotein must be the key component of the oxidase. They also raised the question of whether the two pathways competed directly with each other or were regulated in vivo by some controlling switch. The field has certainly advanced significantly in the 40 years since these proposals, but it is interesting to note how close Bendall & Bonner's (15) suggestions match the most recent information on the protein's crystal structure (112).

Non-protonmotive complex: a respiratory chain complex that does not translocate protons

GENERAL CHARACTERISTICS OF CYANIDE-INSENSITIVE RESPIRATION

Following from Okunuki's (93) work showing that the second oxidase branches from the main respiratory pathway on the substrate side of cytochrome *c*, numerous investigations have confirmed not only that this is the case, but also that the pathway branches at the level of the ubiquinone pool (105), consistent with the oxidase being non-protonmotive (87). **Figure 1** shows a generally accepted scheme of the respiratory chain, including the location of AOX along with the currently accepted crystal structures of the four major respiratory chain complexes (complexes I–IV) and the ATP synthase (complex V). (For a detailed description of the composition of these complexes in addition to the numerous internal

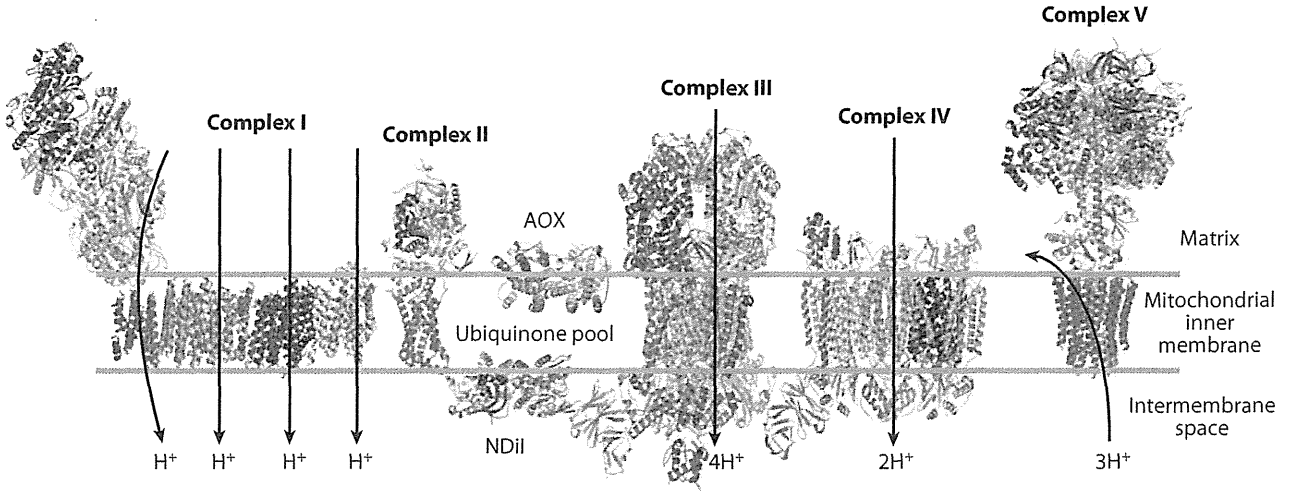

Figure 1

The mitochondrial respiratory chain. The major mitochondrial respiratory complexes are shown as crystal structures where known: complex I, NADH dehydrogenase [Protein Data Bank (PDB) 3M9S (33)]; complex II, succinate dehydrogenase [PDB 3VR8 (113)]; complex III, cytochrome bc_1 [PDB 3H1J 72 (60)]; complex IV, cytochrome *c* oxidase [PDB 10CO (139)]; trypanosomal alternative oxidase [PDB 3VV9 (112)]; yeast NADH dehydrogenase [PDB 4G9K (59)]; and complex V, ATP synthase [F_0, PDB 1C17 (99); F_1, PDB 1E79 (48)]. The stator has not been included, but structures can be found at PDB 2A7U (134) and PDB 1L2P (30).

and external NADH dehydrogenases within the plant respiratory chain, see Reference 79.)

The elegant spectrophotometric studies of Bendall & Bonner (15) clearly demonstrated that the AOX pathway does not contain any chromophores or flavoproteins, and later electron paramagnetic resonance (EPR) studies confirmed that no unique iron-sulfur protein is associated with the oxidase. However, the pathway's ability to reduce oxygen to water requires a transition metal (such as iron), and this idea was supported by the finding that metal chelators (such as primary hydroxamic acids) potently inhibit cyanide-insensitive respiration (109). Minagawa et al. (81) provided the first compelling evidence that iron is required for AOX synthesis, and this was later confirmed by Ajayi et al. (6) using recombinant TAO expressed in *Escherichia coli*.

Although there have been numerous attempts to purify AOX from a variety of sources (15, 18, 23, 34, 35, 57, 66, 91, 103, 140), none could provide definitive experimental evidence about the nature of the transition metal until the advent of recombinant DNA technology. Following Rhoads & McIntosh's (100) isolation of the first cDNA encoding the *AOX* gene, Berthold et al. (20) overexpressed the *Arabidopsis rAOX* gene in *E. coli*, and EPR analysis revealed the presence of a hydroxo-bridged diiron protein at the heart of the oxidase. Later, Moore et al. (88) also found such a signal in isolated mitochondria, purified protein, and recombinant protein. However, Kido et al. (67), using purified TAO protein, were the first to directly demonstrate that AOX contains iron.

The proposal that AOX contains a binuclear nonheme diiron protein initially arose from the modeling studies of Siedow and colleagues (89, 115). Siedow et al. (115) modeled the AOX active site on those found in the diiron group of proteins, such as methane monooxygenase (MMO) and the R2 subunit of ribonucleotide reductase (RNR). The active sites of these proteins contain a four-helix bundle—a common structural element for this group—that acts as a scaffold to bind the binuclear diiron center. In general, the two iron atoms are ligated by four highly conserved glutamate/aspartate residues and two histidine residues, the arrangement of which yields a characteristic signature motif.

MMO: methane monooxygenase

RNR: R2 subunit of ribonucleotide reductase

Although the Siedow et al. (115) model correctly identified AOX as a diiron carboxylate protein, Andersson & Nordlund (11) reassessed this model in view of the finding that the predicted order and length of the helices in the four-helix bundle were substantially different from those of other diiron carboxylate proteins. The Andersson & Nordlund model (11), later refined by Berthold et al. (17), was based on Δ^9-desaturase and thereby resulted in an arrangement of the metal ligands that was closer to that observed in the R2-type diiron proteins than to that predicted by Siedow et al. (115). More important from a structural perspective, however, was that the revised model contained the evolutionarily conserved protein fold observed in all other diiron proteins and additionally included a hydrophobic crevice leading from the membrane-binding region toward the diiron center, presumably acting as the substrate-binding site (17).

The general consensus from such homology modeling is that AOX is an integral (~32-kDA) interfacial membrane protein that contains a nonheme diiron carboxylate active site and interacts with a single leaflet of the lipid bilayer by two short hydrophobic helices (19) in a manner comparable to prostaglandin H1 synthase (96), squalene cyclase (132), and CLK-1 (14). This model is supported by spectroscopy and extensive site-directed mutagenesis studies (6, 7, 20, 44, 90). Recent reference to the Protein Data Bank data sets (**http://pfam.sanger.ac.uk**) reveals that AOXs are currently the largest group within this family of proteins, being present in at least 270 species and having 580 lodged sequences to date.

Plant AOX has also been predicted to be homodimeric, as is the case for prostaglandin synthase, squalene cyclase, and probably CLK-1 (see 14, 19, 96, 132). Interestingly, homodimers have been proposed to be not universal within the AOX group, as fungal and other nonplant AOXs lack the highly conserved cysteines found in plant AOXs (123). Dimerization does result in constraints on subunit orientation, however, because each hydrophobic domain of each monomer must be within the confines of the membrane (17), and in the case of the plant enzyme, at least, if the redox-active cysteines do play a role in dimerization, then they must be oriented such that the cysteines of each monomer can interact with one another.

CLK-1: a small mitochondrial diiron carboxylate enzyme involved in the penultimate step of ubiquinone synthesis

As indicated above, one of the ultimate goals in studying the structure of AOX has been determining a protein crystal structure at sufficient resolution to detect the active site and membrane-binding regions. Although attempts to purify the oxidase from a variety of tissues resulted in purified protein, in general, the lack of yield and relative instability at room temperature have hampered attempts to crystallize the protein (5, 15, 18, 23, 34, 35, 57, 66, 91, 103, 140). A word of caution should be noted, however, with respect to crystallographic structures: Although they are important for an understanding of what the protein looks like, they do provide only a snapshot of the protein in that particular condition and do not necessarily provide full or correct structural details.

Functional expression of TAO (45, 91) and *Arabidopsis thaliana* AOX (AtAOX) (20) at high levels in heme-deficient *E. coli* membranes led to purification protocols that resulted in highly active proteins with remarkable stability. The use of an *E. coli* Δ*hemA* mutant strain that lacks cytochromes *bo* and *bd* arose from the earlier studies of Kumar & Soll (72), who discovered that AtAOX expression in this strain rescues aerobic respiration. More recently, Kido et al. (67) refined earlier attempts (45, 91) to overexpress recombinant TAO and developed purification protocols that resulted in a purified protein of sufficient yield and purity to enable the first report of an AOX crystal (68).

Purified protein has been used not only for crystallization but also in kinetic and spectroscopic studies. Kinetic results have provided some interesting molecular insights into how AOX, a simple ubiquinol oxidase, can compete effectively with other oxidases. For instance, although the calculated specificity constant (K_{cat}/K_m) for TAO is comparable to that of other oxidases, such as cytochrome *bo* (107), it is outcompeted by the cytochrome bc_1 complex (37). As Kido et al. (67) rightly point out,

caution should be exercised in interpreting such results because they are performed under non-physiological conditions and substrate concentrations; nevertheless, these results do reveal that AOX is both kinetically and thermodynamically competent to compete with other oxidases in the respiratory chain. The purity and stability of the recombinant protein have also enabled Fourier transform infrared spectroscopy (FTIR) studies (74), which not only confirmed that AOX is indeed a diiron carboxylate protein (in that it revealed clear signals that could be attributed to carboxylate and histidine residues that change during a redox cycle) but also revealed a sharp band that was tentatively attributed to the loss of a tyrosyl radical (74).

OVERALL THREE-DIMENSIONAL STRUCTURE OF AOX

Molecular modeling using MMO, RNR, or Δ^9-desaturase predicted the presence of a four-helix bundle at the AOX core (19), a characteristic feature of diiron proteins. The TAO crystal structure (112) determined at 2.85-Å resolution indeed confirms that AOX is a diiron carboxylate protein and is dimeric (**Figure 2*a***). Each monomer comprises six long helices (α1 to α6) and four short helices (αS1 to αS4) arranged in an antiparallel fashion, with helices α2, α3, α5, and α6 forming a four-helix bundle (**Figure 2*b*,*c***). Within the dimer (**Figure 2*a***), the two monomers are related by a twofold axis approximately perpendicular to the bundle, comparable to that found in prostaglandin H synthase (96) and squalene cyclase (132), as initially predicted by Andersson & Nordlund (11) and Berthold & Stenmark (19). Helices α2, α3, and α4 of one monomer and α2*, α3*, and α4* of the other (where the asterisk donates the helix of a neighboring monomer) build a dimer interface (**Figure 2*b***). Within the dimer interface, six residues [His-138, Leu-142, Arg-143, Arg-163, Leu-166, and Gln-187 (TAO numbering; see **Figure 3**)] are universally conserved across all known AOX sequences, and eight residues (Met-131, Met-135, Leu-139, Ser-141, Arg-147, Leu-156, Arg-180, and Ile-183) are highly conserved, indicating that a dimeric structure is common to all AOXs. This is obviously in contrast to earlier suggestions that a dimeric structure is not universal (27, 51, 121, 123). The fact that the dimer interface sequence is so highly conserved also lends credence to the notion that dimer formation is not an artifact of crystallographic conditions.

Of particular importance was the finding that, even though the first 30 amino acids in the N-terminal region are not resolved in the structure owing to faint electron density, it is apparent from the crystal structure that the N-terminal arm of one monomer extends into the other monomer (**Figure 2*b***), suggesting that the N-terminal region is important for dimerization. Given that the plant N-terminal

Figure 2

Structure of the trypanosomal alternative oxidase (TAO). Long helices are labeled α1 to α6. Diiron and hydroxo atoms are shown as magenta spheres. (*a*) Surface representation of the dimeric structure viewed roughly perpendicular (*left*) and parallel (*right*) to the helix axes. Helices are shown as ribbons. Except for the N-terminal arm, each monomer is shaped as a compact cylinder (50 × 35 × 30 Å), and there are no significant structural differences among monomers in the asymmetric unit. A large hydrophobic region is visible on one side of the dimer surface; this region is formed by α1 and α4 plus the C-terminal region of α2 and the N-terminal region of α5 from both monomers and is inserted into the membrane to approximately 14 Å. (*b*) Dimer interaction with the membrane. Helices α1 to α6 are associated with chain A, and helices α1* to α6* are associated with chain B (asterisks indicate helices of the neighboring monomer). (*c*) Location of the diiron and hydroxo atoms within the four-helix bundle of one monomer (asterisks indicate helices in chain B). (*d*) Structure of the active site. Diiron and hydroxo atoms are shown as spheres, and four glutamate and two histidine residues important for diiron binding are shown as green sticks. The location of the redox-active Tyr-220 within 4.7 Å of the active site is also shown as a green stick. Carbon is shown in green, nitrogen in blue, and oxygen in red. Numbering refers to the *Trypanosoma brucei* sequence. (*e*) Schematic representation of the active site. (*f*) Hydrogen bond network within the diiron active site. Solid lines show coordinate bonds to the diiron center; dashed lines show hydrogen bonds. His-165 forms hydrogen bonds with Glu-123 and Asn-161. His-269 forms hydrogen bonds with Glu-213 and Glu-162. Asn-161, which is situated in the center of the hydrogen network, forms additional hydrogen bonds with Tyr-246 and Asp-265.

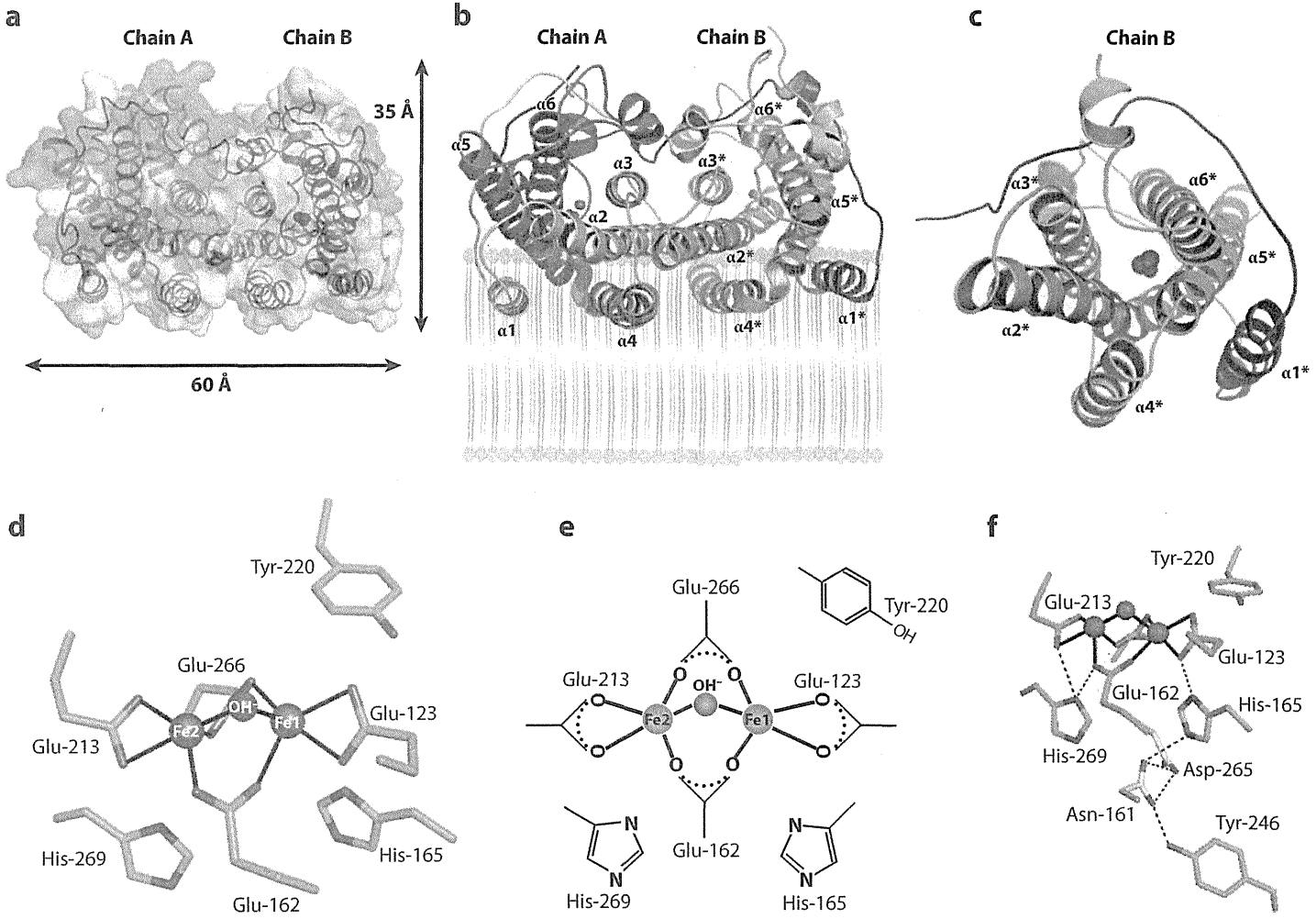

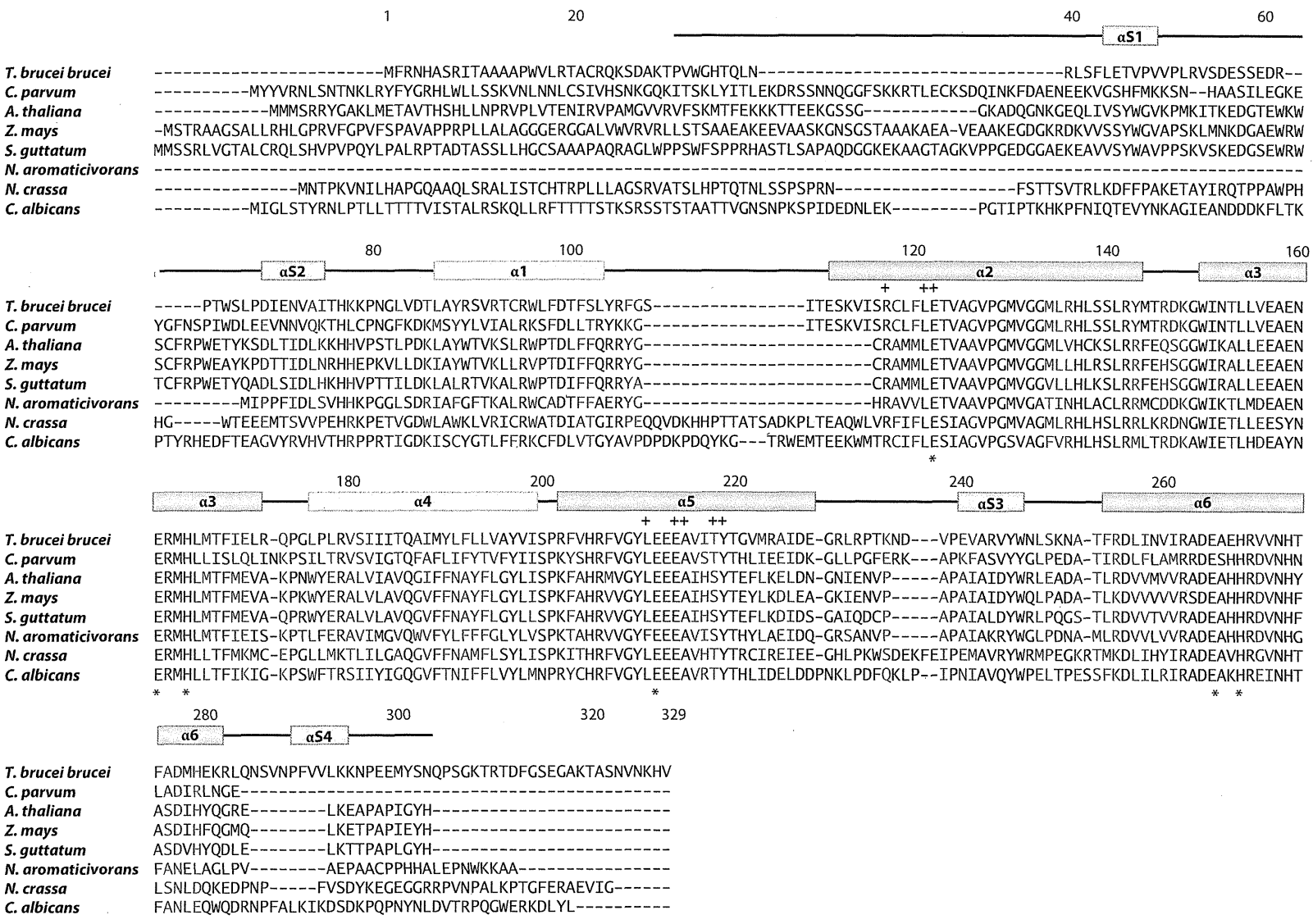

regions tend to be slightly longer than those of trypanosomes, it is interesting to speculate that the redox-active cysteines are oriented in a manner that enables disulfide linkages (121).

Additional important structural information includes the finding that a large hydrophobic region is visible on one side of the dimer surface; this region is formed by helices α1 and α4 plus the C-terminal region of α2 and the N-terminal region of α5. Because this region is present in both monomers and the opposite side of the dimer surface is relatively hydrophilic, we proposed that the dimer is bound to the inner membrane via this hydrophobic region in an interfacial fashion (**Figure 2*a,b***) (112). In support of this idea, basic residues are distributed along a boundary between the hydrophobic and hydrophilic regions of the dimer surface. As shown in **Figure 3**, these residues are conserved across all amino acid sequences of the membrane-bound AOXs, and their locations make them ideal candidates to interact with the negatively charged phosphate head groups on the phospholipid membranes, as previously predicted (11). Importantly, the crystal structure is consistent with the constraint identified by Berthold et al. (17)—namely, that the subunits are oriented in such a way that the hydrophobic domains of each subunit are in the membrane. Given that the N-terminal region of each monomer interacts with its neighbor, the cysteines of each monomer are likely oriented such that they can interact with one another.

Resolution of the Active Site

Previous models of the AOX active site included a hydroxo bridge between the two irons on the basis of a lack of spectroscopic features above 340 nm and a small value of the exchange coupling constant (20, 115). Within the diiron active site, the average distance between the two irons is 3.16 Å, which is also consistent with a single hydroxo bridge (**Figure 2*d***). The active site is located in a hydrophobic environment buried deep within the molecule and comprises the diiron center, four universally conserved glutamate resides, and two universally conserved histidine residues (**Figure 2*d***). In addition to the hydroxo bridge, the two irons are bridged by two glutamate residues, as predicted by Andersson & Nordlund (11), and furthermore are coordinated in a bidentate fashion by two glutamate residues. This results in a five-coordinated diiron center with a distorted square pyramidal geometry (**Figure 2*d***).

The most distinctive feature of the diiron active site in the crystal structure in its oxidized state, however, is that both histidine residues are too far away from the diiron center to coordinate with the two irons. At first glance, such a primary ligation sphere is not consistent with other diiron proteins. For instance, diiron active sites of soluble diiron proteins with known structures, such as Δ^4 acyl carrier protein desaturase (53), MMO (106), RNR (92), and rubrerythrin (64), are all coordinated by at least one if not two histidine residues, and hence AOX is somewhat unusual in the composition of its primary ligation sphere. However, it should be noted that not only did the reduced-minus-oxidized FTIR difference spectra of purified TAO confirm the presence of signals that could be attributed to carboxylates, but also, equally importantly, upon reduction two of these carboxylates

Figure 3

Multiple alignment of AOX amino acid sequences. This alignment was produced from eight amino acid sequences from *Trypanosoma brucei brucei*, *Cryptosporidium parvum*, *Arabidopsis thaliana*, *Zea mays*, *Sauromatum guttatum*, *Novosphingobium aromaticivorans*, *Neurospora crassa*, and *Candida albicans*. The secondary structure elements identified in the trypanosomal alternative oxidase (TAO) structure are also shown. Helices α1 and α4, which form the hydrophobic region on the AOX molecular surface and are involved in membrane binding, are shown in yellow; helices α2, α3, α5, and α6, which form the four-helix bundle accommodating the diiron center, are shown in cyan. Amino acid residues that coordinate the diiron center and those that interact with the inhibitor are indicated by asterisks and plus symbols, respectively. Red, purple, and blue letters denote residues conserved in all eight of the organisms, in six or seven of the organisms, and in four or five of the organisms, respectively.

became protonated and peaks appeared that could be attributed to histidine residues (74). The crystal structure is therefore consistent with an active site in its oxidized form that contains carboxylate ligands but not histidine ligands. The histidine residues do, however, form hydrogen bonds with Glu-123, Asn-161, Glu-162, and Glu-213. Asn-161 is at the center of a hydrogen bond network that includes Tyr-246 and Asp-265 (112). These residues are again universally conserved, and, as is the case with RNR diiron proteins, the hydrogen bond network may be important for stabilization of the active site. Additionally, within 6 Å of the diiron center, other highly conserved hydrophobic residues include Leu-122, Ala-126, Leu-212, Ala-216, and Tyr-220 (see **Table 1**).

Role of Tyrosines

In RNR, a highly conserved tyrosine (Tyr-122) plays a critical role in electron transport (108), and similar roles for tyrosines have been suggested for AOX (2). Scrutiny of **Figure 3** reveals that although there appear to be four conserved tyrosine residues, only three of these (Tyr-198, Tyr-220, and Tyr-246) are universally conserved across all amino acid sequences of membrane-bound AOXs, including the plastid AOX (75). Tyr-198 has been proposed to be involved in ubiquinol binding (85), although its mutation does not lead to a complete loss of activity (10, 29, 90) (see **Table 1**) and crystal structure analysis of TAO indicates that it is separated from the diiron center by at least 15.8 Å (**Figure 4*a***). It is located on the C-terminal portion of helix α4 and forms a hydrogen bond with a conserved His-206 protruding from the N-terminal portion of helix α5. Such a position suggests that it probably stabilizes the structure of the oxidase rather than being directly involved in ubiquinol binding.

Although Tyr-246, which is located on helix α5, is within electron tunneling distance of the diiron center (9.7 Å) (95), it is more likely involved in the hydrogen bond network than in electron transport because it is only 3.1 Å from Asn-161 in helix α3 (**Figure 2*f***). This notion is also supported by the finding that Tyr-246-Ala mutants retain some activity (90), which would not be the case if the residue were essential for electron transfer. Tyr-220, however, is buried deep within the four-helix bundle, within 4.7 Å of the diiron center (**Figure 4*a***), making it the most likely candidate for the amino acid radical proposed to be involved in the AOX catalytic cycle (2) (see Catalytic Mechanism for the Reduction of Oxygen to Water, below). Indeed, Tyr-220 is universally conserved across all AOXs sequenced to date (75), and mutational analyses have unequivocally demonstrated that this residue is essential for the enzymatic activity of all AOXs (7, 90).

Of particular interest is the finding that in AOX, Tyr-220 is located on helix α5 (**Figure 4*b***), in contrast to the redox-active Tyr in RNR (**Figure 4*c***). In AOX, Phe-169 is the amino acid residue equivalent to Tyr-122 in RNR based on a comparison of their structures and amino acid sequences. However, close inspection of both structures reveals that Tyr-220 (**Figure 4*b***) occupies the corresponding positions of Tyr-122 in RNR (**Figure 4*c***). In contrast, RNR Phe-212 occupies the position equivalent to TAO Tyr-220 in both amino acid sequence and structure. As shown in **Figure 4**, the complementary positions of the two amino acid residues found in AOX (**Figure 4*b***) and RNR (**Figure 4*c***) are also observed in bacterioferritin (Tyr-58 and Leu-101; **Figure 4*d***) and rubrerythrin (Leu-60 and Tyr-102; **Figure 4*e***). It is interesting to speculate on whether the position change of Tyr-220 in AOX (**Figure 4*b***) deep within the hydrophobic core of the protein renders it much more resistant (78, 142) to the antiproliferative effects of agents such as nitric oxide (21) in contrast to the susceptibility of RNR (class 1a and 1b) to this agent (42). The fact that the RNR in *Chlamydia* lacks the stable tyrosine radical site and is insensitive to nitric oxide supports this suggestion (54).

Ubiquinol-Binding Sites

In addition to containing an active site for the reduction of oxygen to water, AOX must

Table 1 Roles, locations, and effect of mutation of universally conserved AOX residues

SgAOX numbering	TbAOX numbering	Role	Helix number	Respiratory inhibition (%)
Leu-177	Leu-122	Substrate-binding channels 1 and 2	α2	61
Glu-178	Glu-123	*Fe-Fe ligand; substrate-binding channels 1 and 2	α2	100
Ala-181	Ala-126	*Substrate-binding channels 1 and 2	α2	ND
Pro-184	Pro-129	Substrate-binding channel 2	α2	ND
Gly-185	Gly-130	Forms kink in helix α2 (with P129)	α2	ND
Val-187	Val-132	Hydrophobic interaction with helix α6	α2	ND
His-193	His-138	Membrane-binding region/dimer interface	α2	62
Arg-198	Arg-143	Membrane-binding region/dimer interface	α2	ND
Trp-206	Trp-151	Hydrophobic interaction with helix α6	α3	95
Iso-207	Iso-152	Dimer interface	α3	ND
Leu-210	Leu-155	Dimer interface	α3	ND
Glu-213	Glu-158	*Substrate-binding channels 1 and 2	α3	90
Asn-216	Asn-161	*Secondary ligation sphere; hydrogen bond network	α3	90
Glu-217	Glu-162	*Fe-Fe ligand	α3	100
Arg-218	Arg-163	Membrane-binding region	α3	ND
Met-219	Met-164	Dimer interface; interaction with N-terminal arm	α3	ND
His-220	His-165	*Fe-Fe ligand	α3	100
Leu-221	Leu-166	Dimer interface	α3	ND
Pro-230	Pro-175	Dimer interface	—	ND
Gln-242	Gln-187	Dimer interface	α4	94
Tyr-253	Tyr-198	Dimer interface; hydrogen bonds to His-206	α4	53
His-261	His-206	Membrane-binding region	α5	98
Gly-265	Gly-210	Forms kinks in helix α5	α5	ND
Glu-268	Glu-213	*Fe-Fe ligand	α5	100
Glu-269	Glu-214	Interacts with N-terminal arm	α5	ND
Ala-271	Ala-216	*Substrate-binding channel 2	α5	92
Tyr-275	Tyr-220	*Catalytic cycle	α5	100
Ala-295	Ala-243	Hydrophobic interaction with helix α3	αS3	ND
Tyr-299	Tyr-246	Secondary ligation sphere; hydrogen bond networks	αS3	ND
Arg-316	Arg-263	Interaction with helix α5 and N-terminal arm	α6	ND
Asp-318	Asp-265	*Secondary ligation sphere; hydrogen bond network	α6	ND
Glu-319	Glu-266	*Fe-Fe ligand	α6	100
His-322	His-269	*Fe-Fe ligand	α6	100
Asn-326	Asn-273	Interaction with helix α5	α6	ND
His-327	His-274	Interaction with helix α5	α6	ND

Residue numbering refers to either *Sauromatum guttatum* or *Trypanosoma brucei* AOXs (SgAOX and TbAOX, respectively). Asterisks denote residues within 6 Å of the iron atoms. Helix number refers to the numbering of the α-helices given in **Figure 3**. Data expressed in the "respiratory inhibition (%)" column refer to respiratory inhibition as a result of mutation of the respective residue to Ala compared with wild-type rates and are from References 6–8, 10, 20, 29, 44, 90, and 112. ND, no data.

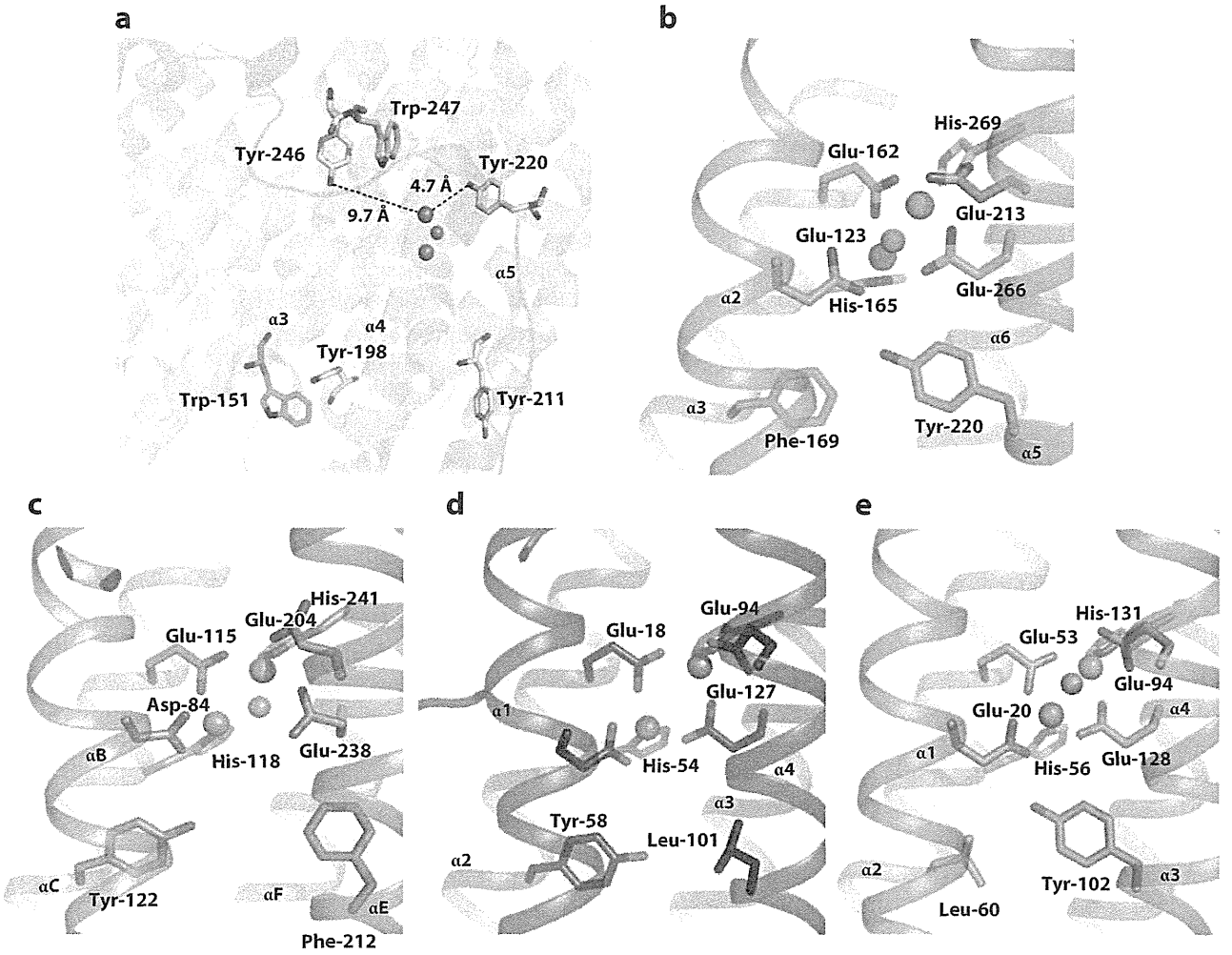

Figure 4

Locations of conserved tryptophan and tyrosine residues and comparison of diiron active sites in AOX with those in other diiron carboxylate proteins. (*a*) Locations of highly conserved tryptophan (*cyan sticks*) and tyrosine (*yellow sticks*) residues within the AOX four-helix bundle. Dotted lines represent distances between Tyr-246 and Tyr-220 and the diiron atoms (Fe1). The other panels show the diiron active sites of (*b*) AOX (*green*), (*c*) the R2 subunit of ribonucleotide reductase (*orange*), (*d*) bacterioferritin (*purple*), and (*e*) rubrerythrin (*cyan*). Oxygen and nitrogen atoms are shown in red and blue, respectively. Diiron, hydroxo, and oxo atoms are shown as colored spheres. Numbering refers to the *Trypanosoma brucei* sequence.

contain a binding site for ubiquinol, the reducing substrate of the protein. Although the structures of several ubiquinone-binding proteins have been determined to atomic resolution (1, 60, 141), the general architecture of this site remains elusive. Despite this, several characteristics thought to be important for ubiquinone binding have been identified. Elucidation of the ubiquinone-binding site in the membrane-associated cytochrome bc_1 complex has resulted in a model comparable to ubiquinone-binding sites in photosynthetic reaction centers in which the ubiquinone-binding pocket is formed by the ends of two transmembrane helices, thus placing the ubiquinone ring near the membrane interface (1, 114). Aromatic residues identified close to ubiquinone-binding regions may interact with the ubiquinone head group in a parallel stacking manner. Additionally, a novel ubiquinone-binding

domain containing a group of polar residues exposed to the membrane interior has been observed that appears to be uniquely conserved among ubiquinol oxidases (1). Furthermore, a sequence analysis of respiratory and photosynthetic complexes that react with ubiquinones identified a putative ubiquinone-binding motif consisting of a histidine-arginine pair and a triad element (41). In addition to these residues (41), serine, arginine, and tyrosine residues have also been identified by biochemical means as being critical for ubiquinone binding in succinate:ubiquinone oxidoreductase (56, 119, 138).

A knowledge of AOX ubiquinol-binding sites is important because they offer the potential of a novel target site for the design of specific inhibitors (104). For instance, in recent years agricultural fungal control has resulted in the development of fungicides specifically targeted to the ubiquinol-oxidation site (Q_o) of the fungal cytochrome bc_1 complex (104). One important group of Q_o site inhibitors that have proved effective in controlling plant pathogens is the strobilurin fungicides, the most widely used of which is azoxystrobin (13). Unfortunately, resistance to this fungicide often develops, making continued application ineffective (71, 135). Although the mechanism for conferring resistance to Q_o fungicides is still controversial (38, 39, 135), there is good evidence to suggest that the addition of inhibitors such as azoxystrobin to fungal pathogens results in a strong induction of AOX (135). Whether the development of AOX can account for field resistance to strobilurins is debatable; nevertheless, it is interesting to speculate on whether inhibition of AOX activity in fungal pathogens increases the sensitivity to commercially available fungicides. Although salicylhydroxamic acid (SHAM) has previously been shown to be ineffective at controlling fungicide resistance when used alongside strobilurin fungicides (13), it should be recognized that SHAM is not specific for AOX in vivo and, furthermore, is a poor inhibitor compared with the antibiotic ascofuranone. Ascofuranone is a ubiquinone analog isolated from the pathogenic fungus *Ascochyta viciae* that specifically inhibits TAO at subnanomolar concentrations (82, 136, 137). For the future development of AOX-specific inhibitors similar to ascofuranone, therefore, a knowledge of AOX ubiquinone-binding sites is critical.

When the plant AOX sequence was initially mapped onto the structure of the Δ^9-desaturase protein, a hydrophobic crevice that reaches down to the diiron center was formed; this crevice was tentatively assigned as a ubiquinol-binding site (11) because a comparable crevice was observed when RNR was used as a template for the oxidase. Such information has been used to model the AOX ubiquinol-binding site (9–11, 17, 89), thereby identifying a hydrophobic pocket between helices α1 and α4 [helices I and III in the Andersson & Nordlund model (11)] that could act as a channel enabling the substrate to gain access to the active site from the membrane-binding domain. Furthermore, the crevice also contained residues, identified in a mutagenesis screen, that result in increased resistance to the presumed competitive inhibitor SHAM (16). Interestingly, these residues flank the extremely well conserved histidine-arginine dyad (41). A number of key residues within this hydrophobic crevice were identified (10) that appeared to be critical for activity, including Tyr-199, Ser-201, His-206, and Arg-207 in addition to Tyr-220, the majority of which are highly conserved. Such mutations suggested that, in addition to the size of the amino acid chain, the presence of hydroxyl, guanadino, imidazole and aromatic groups, and polar and charged residues is important for ubiquinone binding.

An inhibitor-binding pocket was also identified in the TAO crystal structure at 2.6 Å (112) following soaking of the protein in a cryoprotectant solution supplemented with an ascofuranone derivative (**Figure 5*a***). Importantly, the binding pocket is located near the membrane surface between helices α1 and α5 and is lined by 12 highly conserved residues, mutation of which leads to complete loss of enzyme activity. The aromatic head is within 4 Å of the diiron site and is surrounded

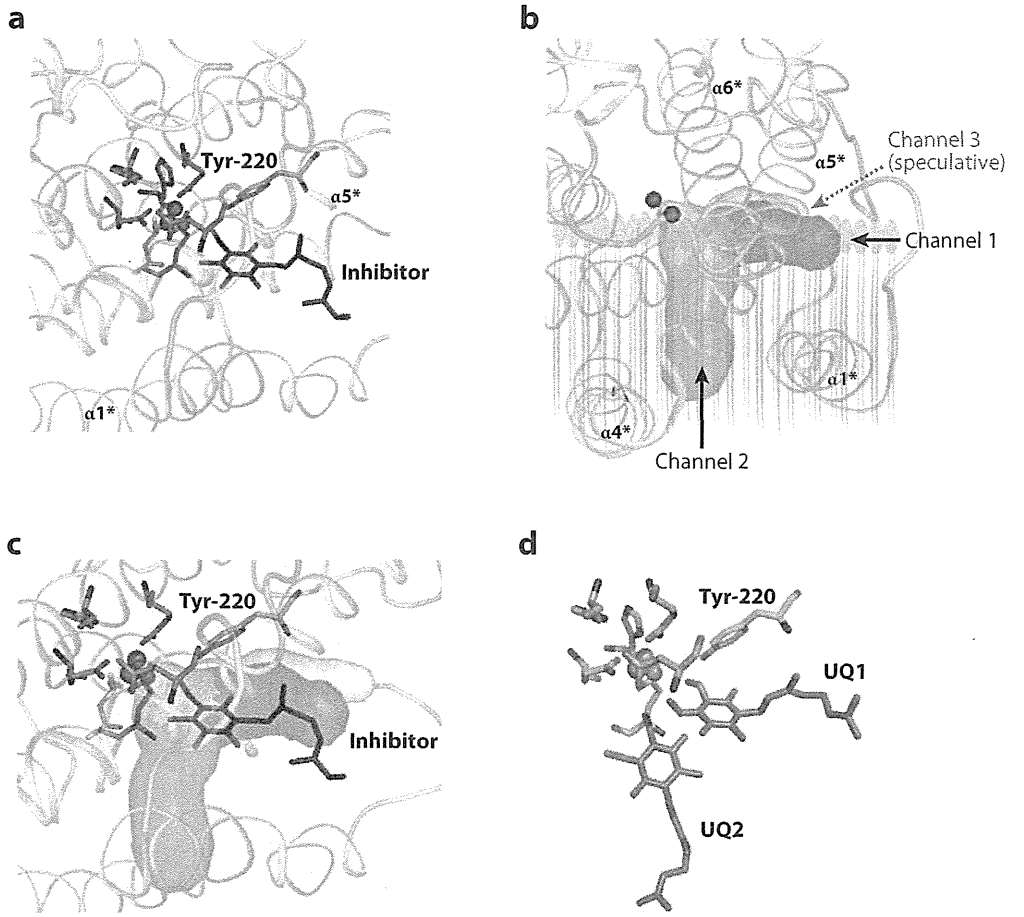

Figure 5

Locations of inhibitor and putative ubiquinol channels in AOX. (*a*) Locations of the diiron active site, Tyr-220, and the inhibitor within the four-helix bundle of a single monomer (asterisks indicate helices associated with chain B). (*b*) Channels connecting the diiron center and the AOX molecular surface, based on a search of the channels conducted using CAVER visualization software (76). A hydrophobic channel (channel 1, *red*) that connects the membrane lipid surface with the diiron core is located between helices α1* and α5* (chain B). Another hydrophobic channel (channel 2, *green*) that connects channel 1 with the membrane hydrophobic core at the diiron center is located between helices α1* and α4*. A more speculative hydrophilic channel (channel 3, *gray*) that connects the diiron center with the protein surface (and is possibly the site of oxygen entry and water exit) is also shown. (*c*) Location of the inhibitor within channel 1 (*red*) based on the structure at 2.6 Å. This binding pocket is located near the membrane surface between helices α1* and α5*, within 4 Å of the diiron center. (*d*) Model of two ubiquinol molecules within channels 1 and 2. Numbering refers to the *Trypanosoma brucei* sequence.

by hydrophobic residues, including Leu-122, Glu-123, Glu-213, Glu-215, Tyr-220, and Glu-266, whereas the isoprenoid tail is surrounded by hydrophilic residues.

In addition to the inhibitor-binding pocket, the CAVER visualization software (76) estimated that there are three possible entrance channels. Channel 1 (**Figure 5*b***), located close and approximately parallel to the membrane surface, links the AOX molecular surface with the diiron center and is the site of the inhibitor-binding pocket. Channel 2 connects channel 1 with the membrane hydrophobic core at the diiron center. The software also suggested the

presence of a third, much more highly speculative hydrophilic channel that links the diiron center with the protein surface and is possibly the site of oxygen entry and water exit. Channel 2 corresponds to the hydrophobic crevice modeled by Andersson & Nordlund (11) and is lined by some of the same suggested residues. The estimated length and diameter of channel 2 (approximately 16 and 5 Å, respectively) are comparable to previous estimates (11), and as indicated in **Figure 5*d***, modeling suggests that it can accommodate ubiquinone. Channel 1 is also of sufficient length and width (13.5 and 4 Å, respectively) to bind ubiquinone, and hence is proposed to be a second substrate-binding pocket. Importantly, residues lining both channels are highly conserved with mutation, particularly of those surrounding the diiron center, resulting in >90% inhibition of activity (112).

Roles and Locations of Universally Conserved Residues

Analysis of multiple sequence alignments has revealed that the four-helix core contains 29 universally conserved residues (**Figure 3**) in addition to the six coordinating ligands (17, 40, 75); **Table 1** summarizes their roles, locations, and effects of mutations. Note that, as mentioned above, mutation of any of the six iron ligands results in complete inhibition of activity (6, 7, 9, 20, 44, 90). Helix α2 contains seven conserved residues in addition to an iron ligand, three of which play a role in substrate binding (Leu-122, Ala-126, and Pro-129) and two of which are important for the membrane-binding region and dimer interface, respectively (His-138 and Arg-143). The roles of Gly-130 and Val-132 are functionally less clear but nevertheless structurally important. Apart from Glu-123, only Ala-126 is within 6 Å of the active site.

Helix α3 contains eight conserved residues in addition to two of the iron ligands. Ile-152, Leu-155, Met-164, and Leu-166 are located within the dimer interface, whereas Arg-163 is in the membrane-binding region. Glu-158 is important for both substrate-binding cavities, whereas Asn-161 is part of the hydrogen bond network and located within the secondary ligation sphere. Trp-151 is involved in a hydrophobic interaction with helix α6 through stacking with Phe-276. Two of these residues—Glu-158 and Asn-161—are within 6 Å of the active site, and mutation of either of these or mutation of Trp-151 results in almost complete loss of activity (**Table 1**).

Helix α4—which, similarly to helix α1, is embedded within the inner membrane—contains two conserved residues, Gln-187 and Tyr-198, both of which reside at the dimer interface. We have previously suggested (10) that both of these residues are involved in ubiquinone binding, but scrutiny of the crystal structure has revealed that both are located at the dimer interface/membrane-binding region and that Tyr-198 (on helix α4) interacts with His-206 on helix α5. Mutation of either residue results in significant inhibition, probably as a result of the breakdown of helix-helix interaction (10, 85).

Helix α5 contains four highly conserved residues in addition to His-206 and Glu-213: Gly-210, which forms a kink in helix α5; Glu-214, which interacts with the N-terminal arm; Ala-216, which is a key component of the substrate-binding cavity; and, of course, Tyr-220, the universally conserved tyrosine that plays a critical role in electron transport. Both Ala-216 and Tyr-220 are within 6 Å of the active site. Small helix αS3 contains two conserved residues: Ala-243, a residue involved in a hydrophobic interaction with helix α3, and Tyr-246, a key residue in the hydrogen bond network. Helix α6 contains four conserved residues, three of which (Arg-263, Asn-273, and His-274) are important for interhelical interaction between helices α5 and α6 and the fourth of which (Asp-265) is part of the secondary ligation sphere and hydrogen bonds with His-269.

In addition to the universally conserved residues, other critical amino acids that are conserved across the majority of species include Arg-95 and Asp-99 (both in helix α1); Arg-118 (in helix α2); Val-209, Glu-215, and Thr-221 (all in helix α5); Trp/Tyr-247 (in helix

αS3); and Glu-258 (in helix α6). Arg-95, Glu-99, and Arg-118 are located within channel 1 and are probably involved in binding the substrate/inhibitor tail. Tyr-246 forms part of the hydrogen bond network linking with Asn-161. Glu-215 has previously been demonstrated to be important for catalytic activity, and although it had originally been proposed to be a member of the primary ligation sphere (8), it is apparent from the crystal structure that it is a key residue within the inhibitor-binding pocket.

Catalytic Mechanism for the Reduction of Oxygen to Water

A considerable number of diiron proteins, including Δ^9-desaturase, MMO, RNR, and rubrerythrin, can reduce oxygen to water as a side reaction to their main respective catalytic activities (43). Gomes et al. (50) suggested that the widespread reactivity of diiron proteins toward oxygen stems from such proteins originating by divergence from a common ancestor whose possible role was an oxygen reductase. Unlike other diiron proteins, however, AOX retains that function, which it carries out through a four-electron reduction of oxygen to water. Although there is considerable experimental evidence in favor of this reaction (2, 74, 84, 85), Bhate & Ramasarma (22) recently suggested that the product of oxygen reduction is actually hydrogen peroxide and not water (i.e., a two-electron reduction process). The fact that even the simplest of diiron proteins, such as rubrerythrin, can reduce oxygen to water rather than hydrogen peroxide—as evidenced by the lack of sensitivity of its activity to catalase and/or superoxide dismutase (50)—does suggest that such a function was a characteristic in the common ancestor of the four-helix diiron protein (86). Hence it is extremely unlikely that AOX, whose ancestor probably derived from the early diiron proteins, has not retained the ability to completely reduce oxygen to water.

Several mechanistic models have been proposed to account for the net oxidation of ubiquinol and the four-electron reduction of oxygen to water by AOX (2, 3, 17, 74). In all of these models, the first step in the catalytic cycle is generally considered to be the binding of oxygen to the diferrous state, which is generally the case for metalloenzymes reacting with oxygen (43, 116). **Figure 6** shows a scheme of the proposed cycle, based on those proposed for MMO (43) and cytochrome *c* oxidase (116, 133).

In this scheme, we propose that the diferrous state is monohydroxo bridged. Before AOX can react with oxygen, the resting oxidized state must undergo a two-electron reduction (probably by ubiquinol) to generate the diferrous center. FTIR studies (74) suggest that a carboxylate shift occurs simultaneously with the generation of this state. We propose that upon binding of oxygen to the diferrous center, two short-lived intermediates are formed prior to the formation of the peroxodiiron species, similar to the reactions observed in other systems (43, 111). The first electron, which is transferred from the diiron core, forms a superoxo species (Fe-O-O*; reaction 1 in the figure) that is immediately reduced to a hydroperoxo intermediate (reaction 2) following the transfer of a proton and electron from a bound ubiquinol, thereby generating a bound ubisemiquinone. This reaction may also be accompanied by a carboxylate shift. Following these transfers, the diiron core rearranges to form a peroxodiiron species, losing water in the process (reaction 3). Homolytic cleavage of the O-O bond (reaction 4) results in an oxodiiron species following extraction of a proton and electron from Tyr-220, thereby generating a tyrosyl radical. The tyrosyl radical is re-reduced by the ubisemiquinone formed in reaction 2. It should be noted that this is one of many possible diiron core arrangements that the diiron site could exist in following the breaking of the O-O bond. The oxodiiron species, which we propose is the resting state, is then reduced by a second ubiquinol, thereby regenerating the diferrous state with the loss of water (reaction 5).

The redox cycle presented in **Figure 6** differs from previous models (2, 116) in that it does not envisage the formation of high-valent

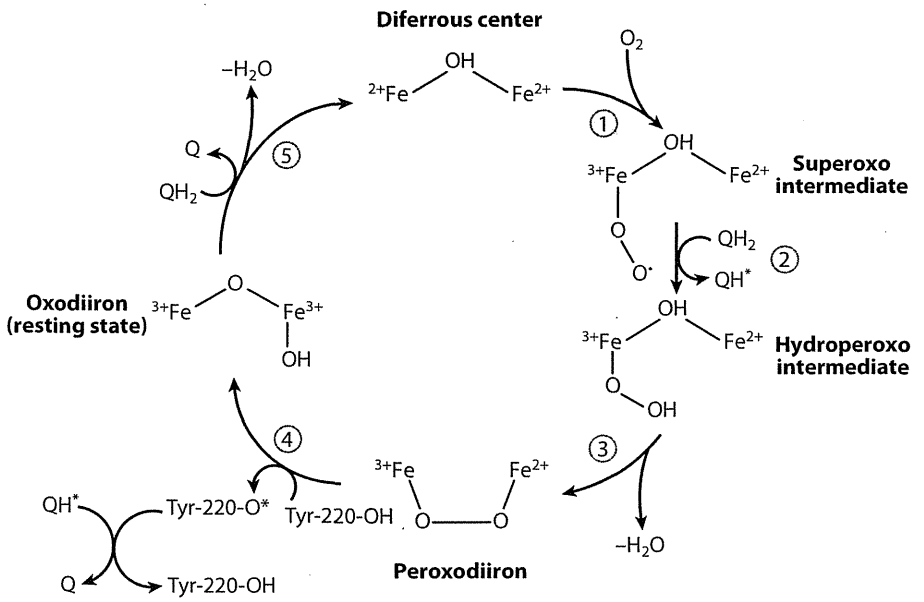

Figure 6

Mechanistic representation of a proposed AOX $O_2/2H_2O$ redox cycle. The binding of oxygen to the diferrous center (reaction 1) results in the formation of two short-lived intermediate species. The diiron core rearranges to form a peroxodiiron species (reaction 3), and following homolytic cleavage of the O-O bond (reaction 4) produces an oxodiiron species as a result of extraction of a proton and electron from Tyr-220. The tyrosyl radical is re-reduced by the ubisemiquinone formed in reaction 2. The oxodiiron species is then reduced by a second ubiquinol, thereby regenerating the diferrous state (reaction 5). (For full details, please refer to the text.)

intermediates but does involve tyrosyl and ubiquinol radicals. Such a model is consistent with the following experimental evidence:

1. The generation of a mixed-valent Fe(II)/Fe(III) EPR signal observed (20) following the introduction of molecular oxygen to a fully reduced sample [interestingly, it was estimated that the mixed-valent state accumulates to a maximum of approximately 5% of the estimated concentration of the AOX monomer (20), which compares favorably with published estimates (111)]
2. The occurrence of a carboxylate shift (74) following the two-electron reduction of the oxodiiron species to form the diferrous state (consistent with reaction 5)
3. The location of Tyr-220 in a catalytically active position (within 6 Å of the bimetallic active site) in the crystal structure (112) and the fact that this residue is universally conserved across AOX species and is essential for catalytic activity (consistent with reaction 4)
4. The fact that a Thr-179-Ala mutant (corresponding to the trypanosomal Thr-124) results in an AOX with reduced catalytic activity and increased apparent K_m for oxygen (29), which, importantly, traps a ubisemiquinone (consistent with reaction 2) (P. Heathcote & A.L. Moore, unpublished results)
5. The inclusion of a single hydroxo bridge and two ubiquinol-binding sites, as predicted from the crystal structure
6. The loss of a sharp negative band at 1,554 cm^{-1} observed by FTIR following the introduction of oxygen to a fully reduced AOX sample, which could arise from the loss of a tyrosyl radical (74) (such a scheme also accounts for short-lived radicals on the basis that ubisemiquinone

generated in reaction 2 rapidly reduces the tyrosyl radical formed in reaction 4)
7. A low-field EPR signal with g values of approximately 16 and a line shape and amplitude comparable to those observed in other diiron proteins (20, 88)
8. The non-proton-pumping nature of AOX

BN-PAGE: blue native polyacrylamide gel electrophoresis

Supercomplex: a multienzyme complex involved in substrate channeling, catalytic enhancement, and the sequestration of reactive intermediates

CysI and CysII: conserved cysteine residues equivalent to Cys-122 and Cys-172 in *Sauromatum guttatum* AOX numbering

NATIVE STRUCTURE OF AOX IN THERMOGENIC PLANTS

Blue native polyacrylamide gel electrophoresis (BN-PAGE) analyses have shown that thermogenic organs of *Arum maculatum* and *Symplocarpus renifolius* contain higher amounts of supercomplex I + III_2 (65, 118) compared with organs in nonthermogenic plants (36). Supercomplex I + III_2 would be beneficial to substrate channeling of the cytochrome *c* oxidase pathway, which contributes to oxidative phosphorylation in mitochondria; however, it may reduce the access of AOX to the complex I–mediated reduced ubiquinone.

Interestingly, Kakizaki et al. (65) recently showed that AOX from thermogenic *A. maculatum* and *S. renifolius* appears as a 150–350-kDa signal on two-dimensional BN-PAGE. Although there are few data on the mitochondrial proteins that interact with AOX, it is possible that AOX, which presumably exists as a multicomplex, primarily catalyzes reducing equivalents from ubiquinone reductases such as alternative NAD(P)H dehydrogenases (65). Based on another recent study, it appears that plant respiratory supercomplexes are affected by the intracellular environment, including oxygen availability and the pH of the mitochondrial matrix (97). Therefore, the native structure of AOX in the mitochondrial respiratory chain may be more dynamic and complex than previously considered.

POSTTRANSLATIONAL REGULATION OF AOX ACTIVITY IN THERMOGENIC PLANTS

Posttranslational regulation of AOX activity in plants is controlled by two interrelated mechanisms: Reduction of an intermolecular disulfide bond results in a more active noncovalently linked dimer (121), and further activation of the reduced AOX occurs by the addition of α-keto acids, particularly pyruvate (80). The mechanism of α-keto acid regulation involves two conserved cysteine residues, CysI and CysII (120, 122). The N-terminal CysI acts as a site for intermolecular bond formation and α-keto acid activation (102, 131), whereas CysII has a less well defined role in α-keto acid activation. SgAOX from the thermogenic *Sauromatum guttatum* is constitutively active in the absence of pyruvate, and the glutamine, aspartic acid, and cysteine (QDC) motif of three adjacent amino acid residues plays a role in its pyruvate-insensitive activity (25, 28). In contrast, another thermogenic plant, *S. renifolius*, expresses a pyruvate-stimulated SrAOX that possesses the glutamine, asparagine, and valine (ENV) motif instead of the QDC motif (94) (see residues 232–235 in **Figure 3**).

The glutamic acid/aspartic acid, asparagine, and valine (E/DNV) motif may be crucial during pyruvate activation in nonthermogenic plants (28). Recent analysis of *AmAOX1e*, one of the seven cDNAs for *A. maculatum* AOX that is abundantly expressed in thermogenic appendices, indicates that the ENV motif is substituted by the glutamine, asparagine, and threonine (QNT) motif, although CysI and CysII residues are well conserved in its primary amino acid sequence (58). In particular, a yeast heterologous expression system demonstrated that AmAOX1e is insensitive to stimulation by pyruvate. Moreover, two *AOX* genes that lack CysI, *NnAOX1a* and *NnAOX1b*, have been isolated from thermogenic *Nelumbo nucifera*, and these gene products may be stimulated by succinate and not by pyruvate (51). *A. maculatum* and *S. guttatum* show transient and rather uncontrolled heat production, whereas *S. renifolius* and *N. nucifera* maintain their flower temperatures. Therefore, it is tempting to speculate that the type of AOX molecule, which is characterized by the presence of a conserved CysI residue and/or E/DNV motif, is related to the phenotype of thermogenic plants.